

Generation of Seed Magnetic Fields in Primordial Supernova Remnants

Hidekazu HANAYAMA¹

hanayama.hidekazu@nao.ac.jp

Keitaro TAKAHASHI²

keitaro@a.phys.nagoya-u.ac.jp

and

Kohji TOMISAKA^{1,3}

tomisaka@th.nao.ac.jp

¹*National Astronomical Observatory of Japan, 2-21-1 Osawa, Mitaka, Tokyo, 181-8588, Japan*

²*Department of Physics and Astrophysics, Nagoya University, Chikusa-ku Nagoya 464-8602 Japan*

³*Department of Astronomical Science, The Graduate University for Advanced Studies [SOKENDAI], 2-21-1 Osawa, Mitaka, Tokyo, 181-8588, Japan*

(Received ; accepted)

Abstract

Origin of the magnetic field ubiquitous in the Universe is studied based on the Biermann mechanism, which is expected to work in the non-barotropic region. We perform a series of two-dimensional MHD simulations of the first generation supernova remnant (SNR) expanding in the inhomogeneous interstellar matter (ISM) and study the Biermann mechanism working in the interior of the SNR. Especially, we pay attention to the relaxation process of electron and ion temperatures via the Coulomb interaction. In the early SNR in which the electron temperature is much lower than the ion temperature, the Biermann mechanism is ineffective, since the gradient of electron pressure is small. Magnetic fields begin to be generated just behind the shock front when the electron temperature is sufficiently relaxed. Assuming the explosion energy of 10^{52} erg, the total magnetic energy generated reaches about 10^{26} erg and does not depend strongly on the parameters of either SNR or ISM. Analytic expression to estimate the magnetic total energy is presented and it is shown this agrees well with our numerical results. Finally we evaluate the expected amplitude of magnetic fields in protogalaxies as $\sim 10^{-19}$ G, which is sufficient for seed fields of the observed galactic magnetic fields.

Key words: magnetic fields — galaxies: high-redshift — methods: numerical — magnetohydrodynamics: MHD — ISM: supernova remnants

1. Introduction

The origin of magnetic fields in the universe has been an active field of modern cosmology and astrophysics (Widrow, 2002; Kulsrud & Zweibel, 2008). Concerning the origin of galactic magnetic fields, which are observationally known to be of order $1\mu\text{G}$, it is argued that dynamo mechanism could amplify and maintain magnetic fields if there were some tiny fields ($\sim 10^{-20}$ G) at the galaxy formation (for example, Lesch & Chiba, 1995). There have been many approaches to the origin of the seed fields such as cosmological scenarios (Turner & Widrow, 1988; Bamba & Yokoyama, 2004; Takahashi et al., 2005; Ichiki et al., 2006) and generation via reionization (Gnedin et al., 2000; Langer et al., 2005). These scenarios predict that the universe is filled with very tiny magnetic fields about $10^{-15} - 10^{-25}$ G and there is a possibility that they could be observationally probed through the detection of delayed high-energy emission from gamma-ray bursts (Plaga, 1995; Ichiki et al., 2008; Takahashi et al., 2008).

In this article, we focus on magnetogenesis in primordial supernova remnant (SNR) via the Biermann mechanism (Biermann, 1950). The Biermann mechanism was also studied in other systems such as the formation of protogalaxies (Kulsrud et al., 1997) and Pop III stars (Xu et al., 2008). The Biermann mechanism is an induction process of magnetic fields and can be derived by combining a generalised Ohm's law with the Maxwell equation (Widrow, 2002),

$$\frac{\partial \mathbf{B}}{\partial t} - \nabla \times (\mathbf{v}_p \times \mathbf{B}) = \frac{m_e c}{e} \frac{\nabla P_e \times \nabla \rho_e}{\rho_e^2}, \quad (1)$$

neglecting the electric resistivity. Here, \mathbf{v}_p , m_e , e , c , P_e , and ρ_e are the velocity of protons, the mass of electrons, the elementary electric charge, the light velocity, the pressure of electrons, and the mass density of electrons, respectively. When we assume $n_e \simeq n_p \simeq n$, $P_e \simeq P/2$, and $\mathbf{v}_p \simeq \mathbf{v}$ where n_e , n_p , n , P , and \mathbf{v} represent the number density of electrons, protons, and ions, the total gas pressure, and the fluid velocity, respectively, equation (1) can be rewritten as

$$\frac{\partial \mathbf{B}}{\partial t} = \nabla \times (\mathbf{v} \times \mathbf{B}) + \alpha \frac{\nabla P \times \nabla \rho}{\rho^2}. \quad (2)$$

The coefficient α is defined as $\alpha \equiv m_p c / 2e \simeq 0.5 \times 10^{-4}$ G sec, where m_p is the mass of protons.

The Biermann mechanism requires a vorticity of plasma gas. The vorticity is generated in the region where the spatial gradients of the pressure and density are not parallel. There are some studies of the interaction of the shock of SNR and interstellar clouds (Klein et al., 1994; Nakamura et al., 2006). These studies revealed that the interaction produces the vorticity efficiently in the shocked region. The interaction of inhomogeneous interstellar medium and the shock of SNR also drives the turbulent motion of the gas, and the vorticity is generated in the bubble of SNR (Balsara et al., 2001). Therefore, primordial SNRs occurred before the galaxy formation can be a candidate of the origin of galactic magnetic fields. Furthermore, it is important to note that primordial supernova explosions play an important role in the magnetogenesis, since the initial mass function (IMF) of population III stars is believed to be

substantially top-heavy (e.g., Abel et al., 2002).

For the generation of the seed fields by the primordial supernova explosions, Miranda et al. (1998) studied the process with multiple explosion scenario of Population III objects. Although their situation considered is more or less similar to ours, their calculations are based on several ad hoc assumptions. First, they calculate magnetic field strength assuming a constant generation rate which is actually dependent on the configuration of the density and pressure gradients. Second, they considered multiple SN explosions, and most of the magnetic fields is produced by the hypothetical objects with a mass $M_0 = 10^6 - 10^{10} M_\odot$, and explosion energy $E_0 = 10^{56} - 10^{60}$ erg. This assumption seems inconsistent with the current understanding of star formation.

In our previous article (Hanayama et al., 2005), we studied the generation of magnetic fields by the Biermann mechanism with realistic two-dimensional magnetohydrodynamic (MHD) numerical simulations. A single SNR with the explosion energy 10^{53} erg was put in inhomogeneous ISM and the generation and evolution of magnetic fields were followed. Then we found the total energy of the magnetic fields to be $10^{28} \sim 10^{31}$ erg depending on the supernova and ISM parameters.

In this article, we present more detailed analysis especially focusing on the temperature relaxation between ions and electrons. When we derived equation (2) from equation (1), we used $P_e \simeq P$ which comes from the assumption that the ions and electrons have the same temperature, $T_e \simeq T_p$. In fact, the temperatures of ions T_i and electrons T_e just behind the shock differ each other and the Rankine-Hugoniot shock jump condition indicates

$$T_i = \frac{3}{16} \frac{m_i v_{\text{bub}}^2}{k_B}, \quad (3)$$

$$T_e = \frac{3}{16} \frac{m_e v_{\text{bub}}^2}{k_B}, \quad (4)$$

where v_{bub} is the shock velocity. Noting that the time scale of the Coulomb interactions between electrons and ions (Spitzer, 1962) is longer than the age of SNR in the early phase, there is a possibility that the electron temperature behind the SNR shock front is much lower than the ion temperature. In this case, the analysis with equation (2) would overestimate the generation of magnetic fields.

For a long time, the temperature relaxation of ions and electrons behind the shock of SNR has been actively discussed by many authors (Itoh, 1978; Cox & Anderson, 1982; Cui & Cox, 1992; Masai, 1994). According to Cox & Anderson (1982), in the unequilibrated region in the early phase of SNR the electron temperature is spatially isothermal. If this is the case, the gradient of electron pressure is negligible and, therefore, the Biermann mechanism is there ineffective. Thus, we have to follow the electron temperature in order to analyze the generation of magnetic fields correctly. This is the main ingredient of the current article.

On the other hand, in the radiative cooling phase, although the electron temperature

is expected to be sufficiently equilibrated to the ion temperature, the radiative cooling process increases its importance with the decrease of the temperature at the shock front, and the thermal structure of the SNR becomes isothermal again (Slavin & Cox, 1992). Then, the Biermann mechanism does not work effectively in the SNR. Therefore, in this study, we focus on the generation of the magnetic fields before the radiative cooling phase.

In section 2, the basic equations for numerical simulation of primordial SNRs, the numerical method, and the initial condition of SNR and its surrounding environment are given. In section 3, we present the results of numerical simulations. We discuss the analytic estimations of the generated magnetic fields in section 4.

2. Models and Methods

2.1. The Basic Equations

The basic equations for our numerical simulations are as follows:

$$\frac{\partial \rho}{\partial t} + \nabla \cdot (\rho \mathbf{v}) = 0, \quad (5)$$

$$\frac{\partial \rho \mathbf{v}}{\partial t} + \nabla \cdot (\rho \mathbf{v} \mathbf{v}) = -\nabla P - \nabla \left(\frac{\mathbf{B}^2}{8\pi} \right) + \frac{1}{4\pi} (\mathbf{B} \cdot \nabla) \mathbf{B}, \quad (6)$$

$$\frac{\partial}{\partial t} \left(E + \frac{\mathbf{B}^2}{8\pi} \right) + \nabla \cdot \left[(E + P) \mathbf{v} + \frac{1}{4\pi} \{ \mathbf{B} \times (\mathbf{v} \times \mathbf{B}) \} \right] = 0, \quad (7)$$

$$\frac{\partial \mathbf{B}}{\partial t} = \nabla \times (\mathbf{v} \times \mathbf{B}) + \alpha \frac{\nabla P \times \nabla \rho}{\rho^2}, \quad (8)$$

where ρ , \mathbf{v} , E , P , \mathbf{B} , and T are the density, velocity, total energy, pressure, magnetic field, and temperature, respectively. Here the total energy of the gas is defined as

$$E = \frac{1}{2} \rho |\mathbf{v}|^2 + \frac{P}{\gamma - 1}, \quad (9)$$

where we fix the value of the adiabatic index γ to 5/3, which is valid in case of the non-relativistic gas. The last term of the right-hand side of equation (8) is called Biermann term and expresses the Biermann effect, where $\alpha = m_p c / 2e$. We assumed the gas is fully ionized and the number ratio of H to He to be 10 : 1. Then the mean molecular weights are $\mu_0 = 14/11 = 1.27$ for nuclei and $\mu_t = 14/23 = 0.61$ for fully-ionized ions and electrons. The number density of the hydrogen atoms is $n_H = (10/11)n$ where n means the number density of the ions ($n_H + n_{He}$). Since we focus on the generation of the magnetic fields in adiabatic expansion phase, we ignore the radiative cooling.

2.1.1. Generation Region of Magnetic Fields

We pay attention to the region where the magnetic fields is generated by the Biermann mechanism. The interaction between the shock wave and the inhomogeneous ISM generates the vorticity. Therefore, especially, in the transition layer of the shock front, the baroclinic term

$(\nabla P \times \nabla \rho)/\rho^2$ is expected to work effectively because the gradient of the pressure is much larger than in other regions. However, the thickness of the layer is much smaller compared with the radius of SNR, and is on the order of, or larger than the ion inertia length of $\sim 10^7/n^{1/2}$ cm (Itoh, 1984). In such a region, although the behaviour of the plasma particle must be considered, it depends on complex processes of the interaction of ions and electrons, and is conventionally studied by particle simulations (Shimada & Hoshino, 2000; Kato & Takabe, 2008). If the electron pressure P_e is not as high as the proton pressure P_p there, the Biermann mechanism may not work effectively. In fact, Shimada & Hoshino (2000) predicted the ratio between the electron and the ion temperatures $T_e/T_i \sim 0.2$ in the transition layer with Alfvénic Mach number of $M_A = 20$. Observationally, the ratio T_e/T_i is less than ~ 0.1 in the transition layer with a shock velocity larger than ~ 2000 km s $^{-1}$ (Rakowski, 2005). Since in the transition layer the electron temperature is expected to be lower than the ion temperature, we ignore the generation process working in the transition layer as long as we consider the early phase of SNR. That is, we only take the Biermann effect in the interior of SNR into account, even if it would lead to an underestimate of magnetic fields. Thus, our analysis is rather conservative.

In our calculation we introduce a switch C_{sw} that discriminates the region of the post shock region where we calculate the Biermann term $(\alpha \nabla P \times \nabla \rho)/\rho^2$ in our one-temperature/one-pressure description. For the search of the boundary between the transition layer and the post shock region, the switch C_{sw} is defined as follows : $C_{\text{sw}} = -1$ in the region of $(\nabla P) \cdot \mathbf{v} < 0$; $C_{\text{sw}} = 1$ in the region of $(\nabla P) \cdot \mathbf{v} > 0$; $C_{\text{sw}} = 0$ in the region of $(\nabla P) \cdot \mathbf{v} = 0$. If the switch C_{sw} is equal to 0 or -1 , then we reduce the Biermann term to zero. In this way, we discuss the generation process of the magnetic fields in the inner region of SNR. Furthermore, since a region with $T_e/T < 0.99$ has isothermal T_e distribution, magnetic generation is ignorable there. Therefore, we restrict the generation region of the magnetic fields to the postshock region with $T_e/T \equiv g \geq 0.99$. Thus, our calculation must give a same result obtained with two-temperature simulation effectively. Then, the induction equation (8) with the relaxation effect of the electron temperature is written as

$$\begin{cases} \frac{\partial \mathbf{B}}{\partial t} = \nabla \times (\mathbf{v} \times \mathbf{B}) + \alpha \frac{\nabla(gP) \times \nabla \rho}{\rho^2}, & (g \geq 0.99 \text{ and } C_{\text{sw}} = 1) \\ \frac{\partial \mathbf{B}}{\partial t} = \nabla \times (\mathbf{v} \times \mathbf{B}). & (\text{others}) \end{cases} \quad (10)$$

2.1.2. Equilibrium Equation of Electron Temperature

We also consider the relaxation of the electron temperature. In the adiabatic expansion phase of SNR, the relaxation equation of electron temperature is derived from the energy equation for the electron gas with the heating effect driven by the Coulomb collision with ions. Here, we ignore the thermal conduction and the radiative cooling. The relaxation equation was given by Itoh (1978), and we convert the formulation according to Cox & Anderson (1982),

$$\frac{df}{dt} = \frac{\partial f}{\partial t} + (\mathbf{v} \cdot \nabla)f = \frac{\ln \Lambda}{80} \left(\frac{n}{T^{3/2}} \right), \quad (11)$$

where $\ln \Lambda$ is the Coulomb logarithm and f is a function of $g = T_e/T$ defined as

$$f = \frac{3}{2} \ln \left(\frac{1 + g^{1/2}}{1 - g^{1/2}} \right) - g^{1/2}(g + 3). \quad (12)$$

After solving equation (11) for f , $g = T_e/T$ can be obtained from an approximate formula

$$g \approx 1 - \exp \left[- \left(\frac{5}{3} f \right)^{0.4} \left\{ 1 + 0.3 \left(\frac{5}{3} f \right)^{0.6} \right\} \right]. \quad (13)$$

We solve equation (11) with other MHD equations and obtain the electron temperature T_e with using equation (13) and the gas temperature distribution T . Since the temperature ratio $g = T_e/T$ takes $1/1836$ just behind the transition region (see equations (3) and (4)), we take a boundary condition as $g = 1/1836$ at the transition region ($C_{\text{sw}} = -1$).

2.2. Numerical Methods

We solve the above equations by a two-dimensional MHD code in the cylindrical coordinates (r, z, ϕ) assuming axial symmetry around the symmetry axis (z). Since we start the calculation from $\mathbf{B} = 0$, it is sufficient to consider only the ϕ -component of the magnetic fields B_ϕ which is generated from the Biermann term.

The code is based on the MHD Roe scheme (Roe, 1981; Cargo & Gallice, 1997) coupled with MUSCL technique (Hirsch, 1990) to achieve the second order spatial and temporal accuracy. We employ improved rotated-hybrid Riemann solvers (Nishikawa & Kitamura, 2008) to overcome so-called Carbuncle phenomenon, which is a numerical instability appeared in the shock wave. Curing $\nabla \cdot \mathbf{B}$ error, we adopted the hyperbolic divergence cleaning given by Dedner et al. (2002) and Matsumoto (2007). We note that equation (11) is also solved by using the fully upwind scheme with MUSCL and Carbuncle cure technique which achieve the second order spatial-temporal accuracy and numerical stability.

The numerical scheme was tested by several problems. We checked the code by comparing with MHD shock tube problems (Brio and Wu, 1988) and the adiabatic SNR with the analytic Sedov solution (Sedov, 1959). In high resolution calculation (4000×4000 grids) of primordial SNR expanding into a uniform ISM (explosion energy E_0 and ISM density n_0 are 10^{51} erg and 0.2 cm^{-3} , respectively), the postshock density peak value of the shock front at 1500 yr after the SN explosion was 95.8% of the analytical value (four times larger than the density of ISM), for example. In addition, we compared our results with those of Nakamura et al. (2006) for the case of interaction of a plane-parallel shock with a cloud to check the robustness of our calculation of the vorticity derived from the induction equation (8). As for the normalized peak value of total circulation Γ in the evolution of the cloud distracted by the planar shock, it is analytically estimated as -1.77 (Klein et al., 1994) for the model of AS8 (see Nakamura et al., 2006). The result of Nakamura et al. (2006) is -2.01 while that of our calculation is -1.61 , and both results are in good agreement with Klein's estimation within 10%.

In computation, our numerical domain covers a region of $128 \text{ pc} \times 128 \text{ pc}$ with 2048×2048 grid points. The grid spacings are $\Delta r = \Delta z = 0.0625 \text{ pc}$ and the length scale of density fluctuation (8 pc, see below) is resolved with 128 grids. This is sufficient for the convergence of the total magnetic energy as we show later. In the simulated region of $128 \text{ pc} \times 128 \text{ pc}$, the average density of ISM is approximately constant even in the dark halo structure (Kitayama & Yoshida, 2005).

2.3. Initial Conditions

We assume inhomogeneous ISM with average number density of $n_0 = 0.2 \text{ cm}^{-3}$ for initial conditions of our fiducial model, and also consider a model with $n_0 = 0.8 \text{ cm}^{-3}$ as a variation. These assumptions are consistent with the previous studies (Kitayama & Yoshida, 2005; Greif et al., 2007), in which they obtained initial conditions for Population III SN sites that were calculated by self-consistent radiative transfer calculations. The scale length of the density fluctuation and the amplitude of the inhomogeneity are not well understood. Recently, Wise & Abel (2008) studied the formation process of HII region around a very massive first star with 3D numerical simulations, and showed the anisotropic expansion and inhomogeneous density structure in the HII region with the scale of $\sim 1 \text{ kpc}$. In their study, the HII region has relatively large density inhomogeneities and the spatial scale of the large inhomogeneity seems to be of the order $10 \sim 100 \text{ pc}$. Therefore, we assume here inhomogeneity with relative density fluctuation $\delta n \equiv (n - n_0)/n_0$ derived from a Gaussian spectrum with concentration around a scale length λ_0 (32 and 64 pc) and amplitude A_0 (0.25 and 0.125), where we assume the power spectrum with a peak at the wave number $k_0 (= 128 \text{ pc}/\lambda_0)$ as $A_0 \exp[-(k - k_0)^2/2\sigma_k^2]/2\pi k$ and set the variance $\sigma_k = 0.5$ to achieve $-1 < \delta n < 1$. Avoiding the biased distribution, a normally-distributed random number in the range from 0.9 to 1.1 is multiplied to the amplitude of δn in Fourier space and a uniformly-distributed random number in the range from 0 to 2π is added to the phase. Then, the number density is given by using δn in real space as $n = n_0(1 + \delta n)$.

For the explosion energy of the supernova, we adopt $E_0 = 10^{52} \text{ erg}$ for the fiducial model (Kitayama & Yoshida, 2005; Greif et al., 2007). This explosion energy corresponds to stars with mass $200 M_\odot$ which explodes as a pair-instability supernova (Fryer et al., 2001). Also we consider a model with $E_0 = 2.5 \times 10^{51} \text{ erg}$ as a variation.

We begin the simulation by adding thermal energy of $E_0 = 10^{52}$ or $2.5 \times 10^{51} \text{ erg}$ to the cells near the origin $(r, z) = (0, 0)$ with Gaussian distribution. Initial distribution of thermal pressure $P_{\text{SN}}(r, z)$ with explosion energy E_0 is defined as

$$P_{\text{SN}}(r, z) = \frac{(\gamma - 1)E_0}{(\sqrt{2\pi}\sigma_{\text{SN}})^3} \exp\left(-\frac{z^2 + r^2}{2\sigma_{\text{SN}}^2}\right), \quad (14)$$

where σ_{SN}^2 represents variance of Gaussian distribution and we assumed $\sigma_{\text{SN}} = 2 \text{ pc}$.

We set the gas density uniform from the origin $(0, 0)$ to 10 pc ($= 5\sigma_{\text{SN}}$) in the radius, assuming the effect of the intense radiation field and stellar wind from a progenitor star. In

Table 1. Model parameters.

Model	λ_0 (pc)	A_0	n_0 (cm ⁻³)	E_0 (erg)
A...	32	0.25	0.2	10 ⁵²
B...	64	0.25	0.2	10 ⁵²
C...	32	0.125	0.2	10 ⁵²
D...	32	0.25	0.8	10 ⁵²
E...	32	0.25	0.2	2.5×10^{51}

addition, to connect the homogeneous region and inhomogeneous region smoothly, δn was replaced by $\delta n'$ where

$$\delta n'(x, y, z) = \left(\frac{\sqrt{r^2 + z^2} - 5\sigma_{\text{SN}}}{10\sigma_{\text{SN}} - 5\sigma_{\text{SN}}} \right)^2 \delta n(r, z), \quad (15)$$

in the region from 10 pc ($= 5\sigma_{\text{SN}}$) to 20 pc ($= 10\sigma_{\text{SN}}$) in the radius.

We summarise taken parameters in table 1.

3. Results

3.1. Dynamical Evolution of SNR

First of all, let us give some basic formulae about dynamical evolution of SNR. The evolution of SNR is divided into the following three phases, (1) free expansion phase, (2) Sedov phase, and (3) radiative cooling phase. The free expansion phase continues until the ejecta sweeps up about the same amount of the mass of ejecta M_{ej} in ISM around SNR. The transition radius from free expansion to Sedov phase R_{Sedov} and the transition time t_{Sedov} are written as

$$R_{\text{Sedov}} \sim 19 \text{ pc} \left(\frac{n_0}{0.2 \text{ cm}^{-3}} \right)^{-1/3} \left(\frac{M_{\text{ej}}}{200 M_{\odot}} \right)^{1/3}, \quad (16)$$

$$t_{\text{Sedov}} \sim 8.7 \times 10^3 \text{ yr} \left(\frac{n_0}{0.2 \text{ cm}^{-3}} \right)^{-1/3} \left(\frac{M_{\text{ej}}}{200 M_{\odot}} \right)^{5/6} \left(\frac{E_0}{10^{52} \text{ erg}} \right)^{-1/2}. \quad (17)$$

In the Sedov phase, the expansion of shock wave is well approximated by a self-similar solution,

$$R_{\text{bub}} \sim \left(\frac{E_0}{\rho_0} \right)^{1/5} t^{2/5}, \quad (18)$$

where R_{bub} is the shock radius at time t after the explosion and ρ_0 is the average mass density of ISM. The shock speed is given as the time derivative of R_{bub} ,

$$v_{\text{bub}} = \frac{dR_{\text{bub}}}{dt} = \frac{2}{5} \left(\frac{E_0}{\rho_0} \right)^{1/5} t^{-3/5}. \quad (19)$$

When the gas at the shock front becomes radiative, a dense shell forms at the outer boundary of SNR. The transition into the radiative cooling phase occurs at the time t_{cool} and the radius R_{cool} where

$$t_{\text{cool}} \sim 5.1 \times 10^5 \text{ yr} \left(\frac{n_0}{0.2 \text{ cm}^{-3}} \right)^{-3/4} \left(\frac{E_0}{10^{52} \text{ erg}} \right)^{1/8}, \quad (20)$$

$$R_{\text{cool}} \sim 120 \text{ pc} \left(\frac{n_0}{0.2 \text{ cm}^{-3}} \right)^{-1/5} \left(\frac{E_0}{10^{52} \text{ erg}} \right)^{1/5}, \quad (21)$$

where we assumed the radiative cooling is dominated by free-free radiation of H and He (Shull, 1980). On the other hand, the time scale of the Compton cooling for the primordial SNR is given as

$$t_{\text{Comp}} \sim 7 \times 10^6 \text{ yr} \left(\frac{1+z}{20} \right)^{-4}, \quad (22)$$

which is larger than t_{cool} for $z \lesssim 30$ in which we are interested. As stated above, in this article, we focus on the generation of the magnetic fields in the Sedov phase ($t_{\text{Sedov}} < t < t_{\text{cool}}$).

In fact, there is another important time scale at which the electrons and ions can be regarded as a one-temperature fluid. The typical time scale is given by the age at which the electron and ion equipartition time just behind the shock front τ_{eq} is sufficiently shorter than the age, that is, $\tau_{\text{eq}} < 0.1t$ (Cox, 1972; Itoh, 1978),

$$t_{\text{relax}} \sim 3.3 \times 10^4 \text{ yr} \left(\frac{n_0}{0.2 \text{ cm}^{-3}} \right)^{-4/7} \left(\frac{E_0}{10^{52} \text{ erg}} \right)^{3/14}. \quad (23)$$

The mean radius of SNR at this time is written as

$$R_{\text{relax}} \sim 45 \text{ pc} \left(\frac{n_0}{0.2 \text{ cm}^{-3}} \right)^{-1/5} \left(\frac{E_0}{10^{52} \text{ erg}} \right)^{1/5}. \quad (24)$$

At this time, the mean temperature of electrons is $\langle T_e \rangle = 0.92 \langle T \rangle$ where the each mean temperature is defined with the ion number density n as

$$\langle T_e \rangle / T_s = \frac{\int_0^{R_{\text{bub}}} n^2 [T_e / T_s] R^2 dR}{\int_0^{R_{\text{bub}}} n^2 R^2 dR}, \quad (25)$$

$$\langle T \rangle / T_s = \frac{\int_0^{R_{\text{bub}}} n^2 [T / T_s] R^2 dR}{\int_0^{R_{\text{bub}}} n^2 R^2 dR}, \quad (26)$$

where T_s represents the gas temperature at the shock front. As already explained, the relaxation of the electron temperature is crucial for the Biermann mechanism.

The above characteristic time scales and radii for the five models adopted here are summarised in tables 2 and 3. Here, t_{end} in table 2 is the time when we stopped the calculation, and R_{end} in table 3 is the corresponding radius of SNR.

Table 2. Time scale for each epoch.

Model	t_{Sedov} (10^3 yr)	t_{relax} (10^4 yr)	t_{end} (10^5 yr)	t_{cool} (10^5 yr)
A...	8.7	3.3	3.4	5.0
B...	8.7	3.3	3.4	5.0
C...	8.7	3.3	3.4	5.0
D...	5.5	1.5	1.7	1.8
E...	17.3	2.4	4.1	4.2

Table 3. Mean radius for each epoch.

Model	R_{Sedov} (pc)	R_{relax} (pc)	R_{end} (pc)	R_{cool} (pc)
A...	19	45	115	133
B...	19	45	115	133
C...	19	45	115	133
D...	12	25	66	67
E...	19	30	93	94

3.2. Generated Magnetic Fields

The evolution of the structure of the gas density and magnetic fields for model A, our fiducial model, is shown in figure 1.

When the blast wave expands into the surrounding inhomogeneous medium and the electron temperature is sufficiently relaxed, the magnetogenesis by the Biermann mechanism starts to work. For this model, magnetogenesis starts when the SNR expands to the radius of ~ 45 pc. At $t = 6 \times 10^4$ yr, the radius of the bubble reaches ~ 60 pc and the anisotropic structure is clearly seen, which is induced by the interaction of shock front and the density inhomogeneity of the ISM. The amplitude of the magnetic field is $\sim 10^{-17}$ G behind the shock front at this time. At $t = 2 \times 10^5$ yr, the shock expands to ~ 90 pc, and the magnetic fields are $\sim 10^{-18}$ G just behind the shock front while they are 10^{-17} G for the inner hot cavity. At $t = 3.4 \times 10^5$ yr, the radius reaches ~ 110 pc and the magnetic fields of $\sim 10^{-17} - 10^{-18}$ G are distributed from the radius of 60 to 110 pc.

Figure 2 shows the distributions of the gas number density, the electron pressure, the magnetic fields and the ratio of the electron temperature T_e to the gas temperature T at $t = 6 \times 10^4$ yr. At first glance, the distributions of the density (upper-left panel) and the electron pressure (upper-right panel) look very similar. However, in fact, the gradient vectors of the density and the electron pressure are not exactly parallel (lower panels), which is necessary for the Biermann mechanism to work. These panels show that the density gradient has the

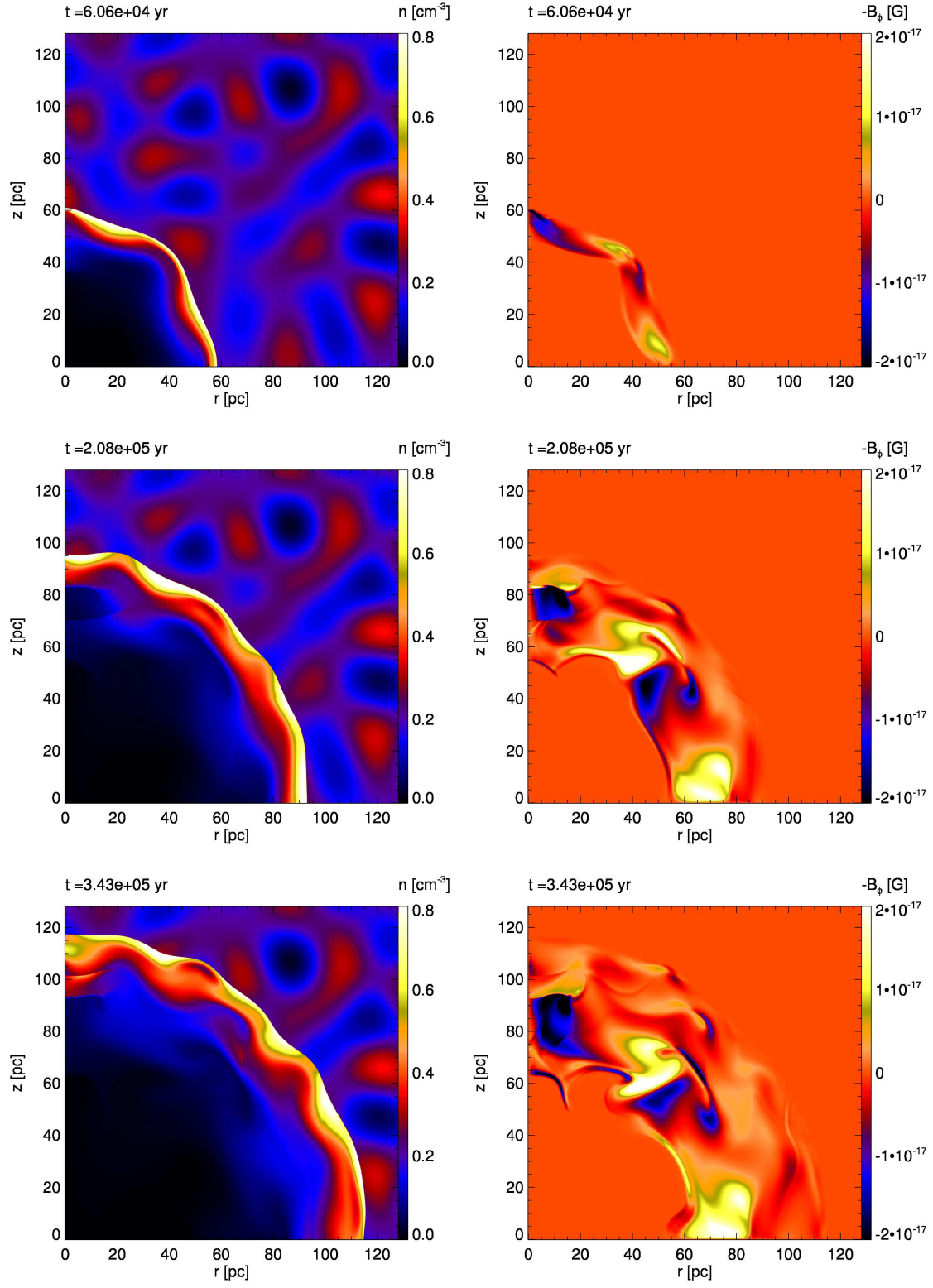


Fig. 1. Distributions of the gas number density (left) and the magnetic fields (right) at $t = 6 \times 10^4$ (top panels), 2×10^5 (middle panels), and 3.4×10^5 (bottom panels) yr for model A.

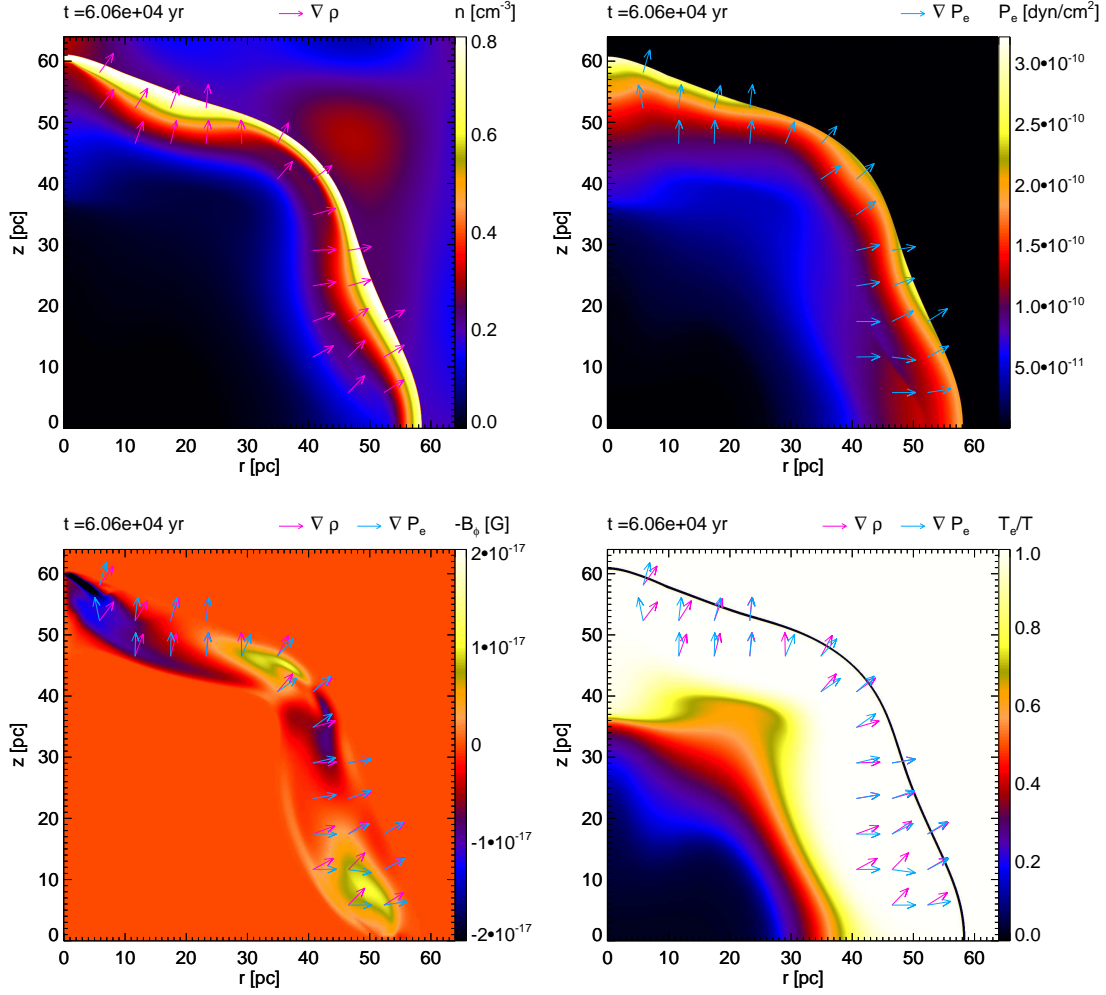


Fig. 2. Distributions of the gas number density (upper-left), the electron pressure (upper-right), the magnetic fields (lower-left), and the ratio of the electron temperature and the gas temperature (lower-right) at $t = 6 \times 10^4$ yr for model A. Red and blue arrows represent directions of the gradients of the density and the electron pressure, respectively.

relatively larger azimuthal component compared with the pressure gradient. This would originate from the density inhomogeneity in ISM. This is consistent with the picture of Nakamura et al. (2006) where it was suggested that the density structure is affected by the distribution of the diffuse cloud, while the pressure is mainly determined by the global structure of the SNR and has more or less radial gradient. Here it should be important to note that magnetogenesis does not occur in the deep interior of the bubble. This is because, as we see in the lower-right panel, the electron temperature has not been relaxed due to low density.

The probability distribution function (PDF) of the magnetic field strength is defined as

$$\Pi(\log |B_\phi|) \equiv \frac{N(\log |B_\phi|)}{N_{\text{cells}}}, \quad (27)$$

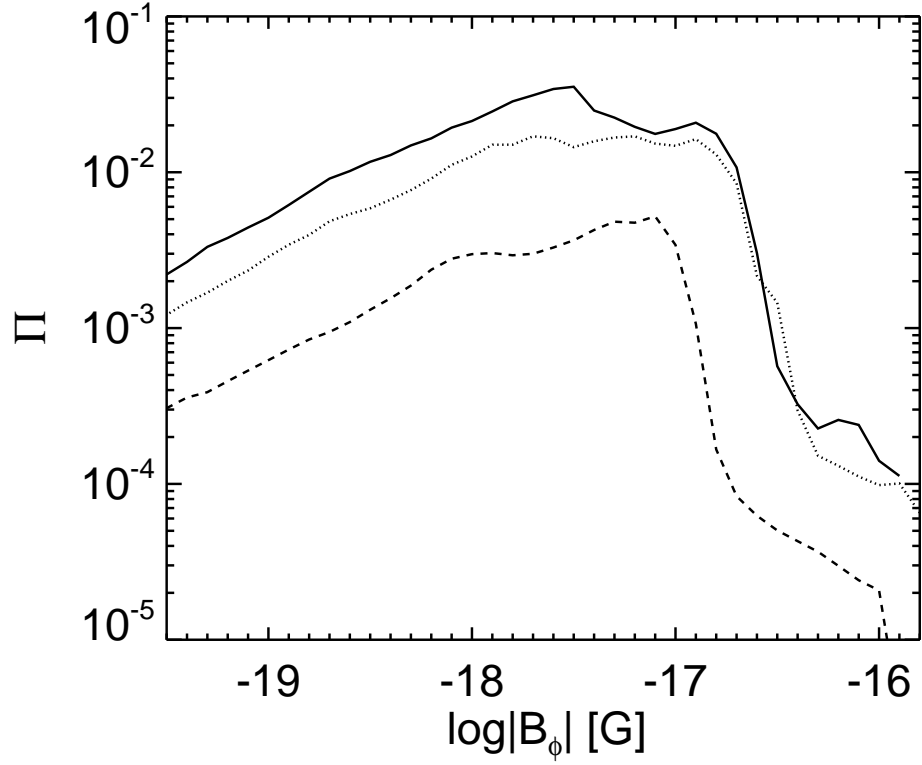


Fig. 3. PDF of the strength of the magnetic fields at $t = 6 \times 10^4$ (dashed line), 2×10^5 (dotted line), and 3.4×10^5 (solid line) yr for model A.

where $N(\log|B_\phi|)$ is the number of cells with magnetic fields B_ϕ and $N_{\text{cells}} = 2048^2$ is the total number of cells. The PDFs at these epochs are shown in figure 3. We can see that the magnetic fields of $\sim 10^{-17} - 10^{-18}$ G are generated at each epoch. The magnetic fields of $\sim 10^{-16}$ G are generated in restricted number of cells, although the population is not so large.

Figure 4 shows the square root of the energy spectrum of the magnetic fields for several times. The energy spectrum of the magnetic fields is calculated by using a definition of shell-averaged magnetic power spectrum $P_M(k)$ derived by Christensson et al. (2001). Fourier series $\mathbf{B}_f(k_r, k_z)$ is written as

$$\mathbf{B}_f(k_r, k_z) = \int_{-L}^L \int_{-L}^L \frac{dr dz}{(2L)^2} \mathbf{B}(r, z) e^{-i \frac{\pi}{L} (k_r r + k_z z)}, \quad (28)$$

where k_r , and k_z represent wave numbers for respective directions in a period $2L$ ($= 256$ pc). We assume $\mathbf{B} = (0, B_\phi, 0)$ in the first quadrant, and the antisymmetric one against the axis in other quadrants. The power spectrum $P_M(k)$ in Fourier space is defined as

$$P_M(k) = \langle \mathbf{B}_f^* \cdot \mathbf{B}_f \rangle, \quad (29)$$

where $\langle \mathbf{B}_f^* \cdot \mathbf{B}_f \rangle$ is the value averaged over the shells with constant $k = |\mathbf{k}|$. Then, the shell-

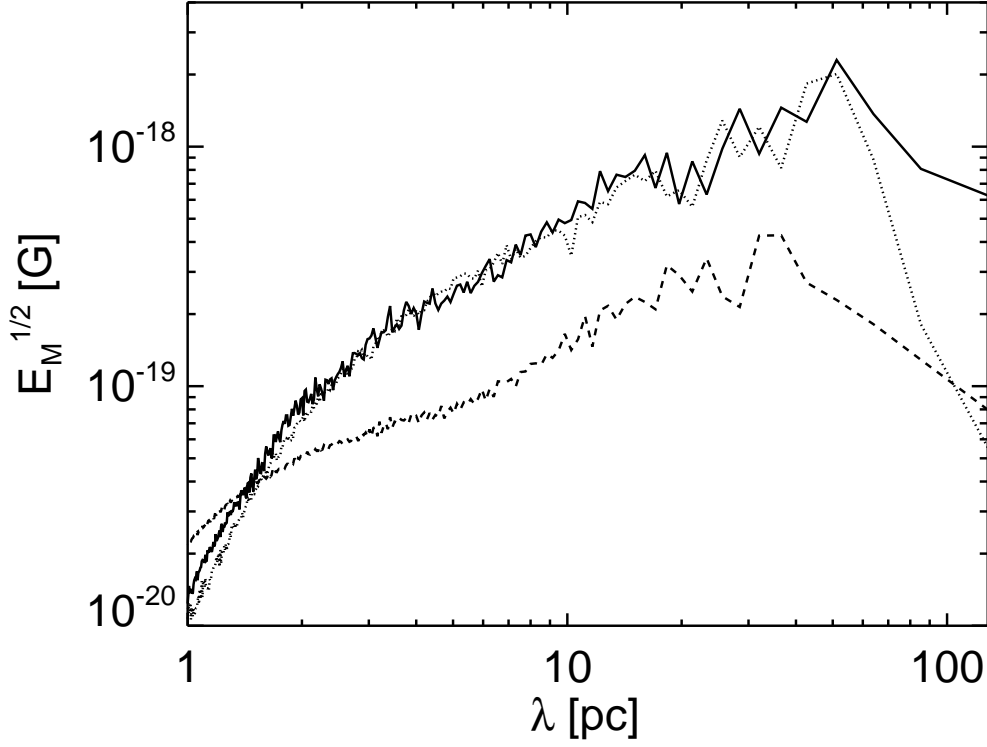


Fig. 4. Square root of the energy spectrum of the magnetic fields at $t = 6 \times 10^4$ (dashed line), 2×10^5 (dotted line), and 3.4×10^5 (solid line) yr for model A.

integrated magnetic energy spectrum $E_M(k)$ is written as

$$E_M(k) = 2\pi k P_M(k). \quad (30)$$

In figure 4, $\sqrt{E_M(\lambda)}$ is plotted against the wave length $\lambda = 2L/k$. At $t = 6 \times 10^4$ yr, the peak value is $\sim 4 \times 10^{-19}$ G, and the corresponding wave length λ_{BP} is 37 pc which is near the scale of the initial fluctuation of ISM, $\lambda_0 = 32$ pc. At $t = 2 \times 10^5$ yr and 3.4×10^5 yr, the spectra are almost identical. The energy spectrum takes the maximum at $\lambda_{BP} = 51$ pc which is nearly equal to $1.5\lambda_0$. We can also see that the generation of magnetic fields completed by $t = 2 \times 10^5$ yr.

The size of the magnetic loop extending in ϕ -direction equals to the typical coherence length appeared in figure 4, $\sim \lambda_{BP}/2$. Then, the radius of the toroidal fields r_t is considered to be $r_t = \lambda_{BP}/4 \sim 1.5\lambda_0/4$, and the coherence length is estimated as $2\pi r_t \sim 1.5\lambda_{BP} \sim 2\lambda_0 \sim 64$ pc at 3.4×10^5 yr. This indicates that the magnetic field is expected to be observed with a 3-dimensional size of $2\pi r_t \sim 64$ pc from our 2-dimensional simulations.

3.3. Comparison of Models

In this subsection, we make a comparison of the results of the five models (A-E) shown in table 1. The PDFs of the magnetic field strength for the five models are shown in figure

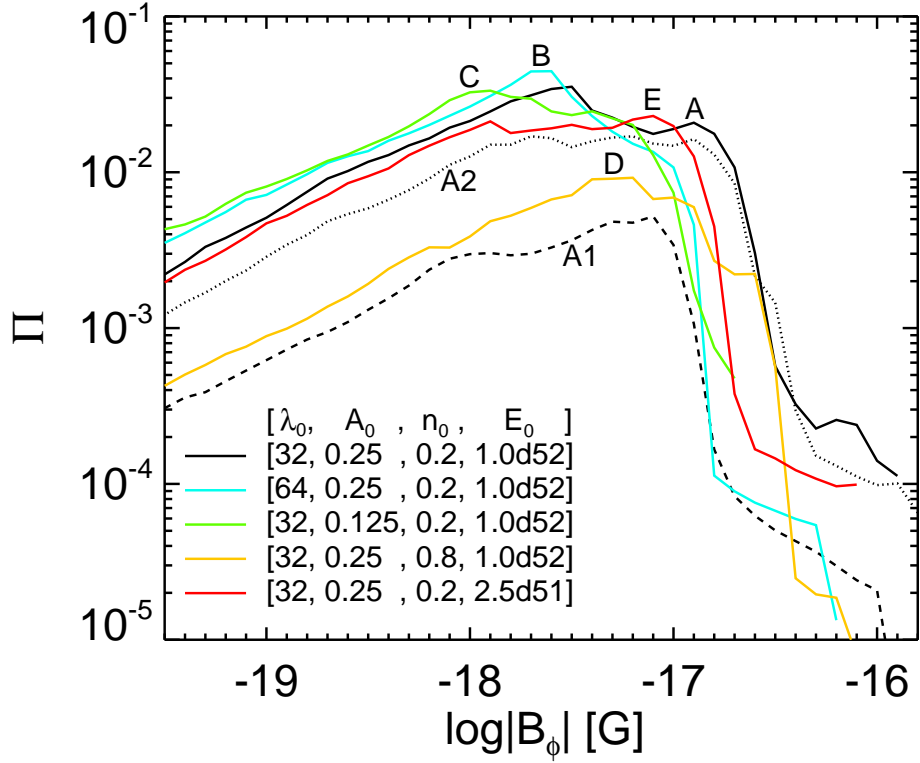


Fig. 5. Comparison of PDFs of the strength of the magnetic fields for each model. Black, blue, green, yellow, and red lines represent the models A ($t = 3.4 \times 10^5$ yr), B ($t = 3.4 \times 10^5$ yr), C ($t = 3.4 \times 10^5$ yr), D ($t = 1.2 \times 10^5$ yr), and E ($t = 4.1 \times 10^5$ yr), respectively. Dashed (A1) and dotted (A2) lines represent $t = 6 \times 10^4$ and 2×10^5 yr for model A.

5. This indicates that the amplitude of magnetic fields are not so different for the variation of our models. Considering the maximum amplitude of $|B_\phi|$ with $\Pi > 10^{-2}$, $|B_\phi(\Pi > 10^{-2})|$ of model A is roughly twice as large as that of models B and C. The radius and large-scale structure for models D ($R = 60$ pc, $t = 1.2 \times 10^5$ yr) and E ($R = 90$ pc, $t = 4.1 \times 10^5$ yr) are similar to those of model A at $t = 6 \times 10^4$ yr (A1, dashed line; $R = 60$ pc) and 2×10^5 yr (A2, dotted line; $R = 90$ pc), respectively. This simply comes from the self-similar evolution of the SNR in the adiabatic phase. Accordingly, we compare the PDF plots of models D and E with curves A1 and A2, respectively. Then, for model D, the PDF of the magnetic fields can be compared with that of model A at $t = 6 \times 10^4$ yr (A1, dashed line). $|B_\phi(\Pi > 10^{-3})|$ of model D at $t = 1.2 \times 10^5$ yr is larger than that of model A at $t = 6 \times 10^4$ yr. This difference comes from the fact that the post shock pressure of model D at $t_{\text{relax}} = 1.5 \times 10^4$ yr is larger than that of model A at $t_{\text{relax}} = 3.3 \times 10^4$ yr because the amplitude of the generated magnetic fields is fundamentally proportional to the pressure gradient. The same argument can be applied to the comparison of model E and model A at $t = 2 \times 10^5$ yr (A2, dotted line). For the population of

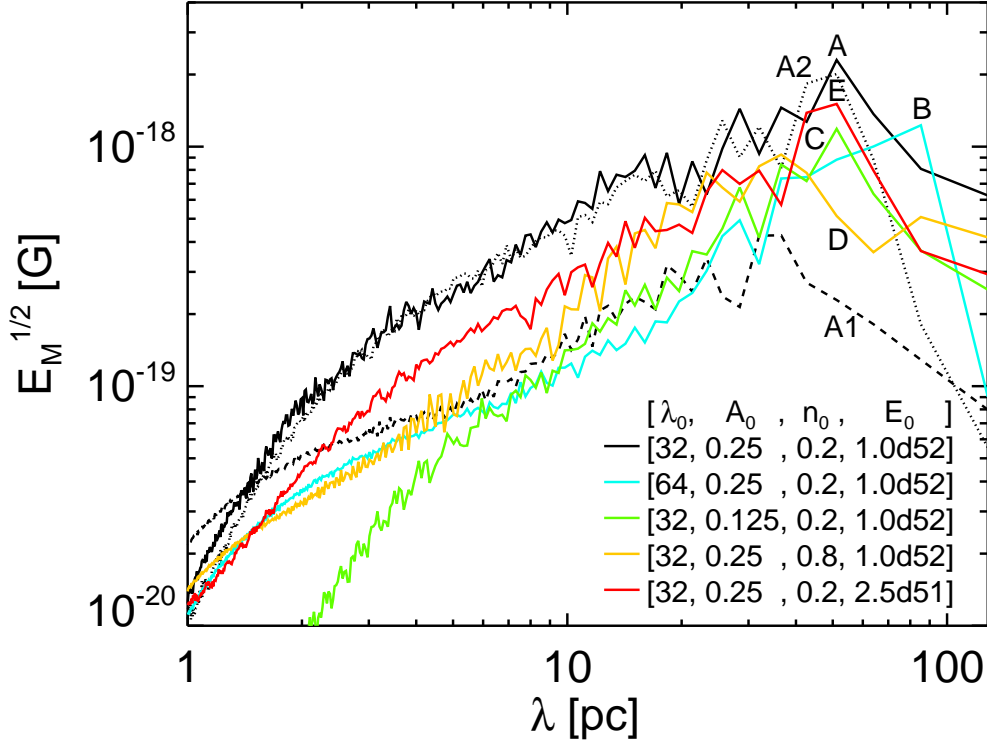


Fig. 6. Comparison of the square roots of the energy spectrum of the magnetic fields for each model. Black, blue, green, yellow, and red lines represent models A ($t = 3.4 \times 10^5$ yr), B ($t = 3.4 \times 10^5$ yr), C ($t = 3.4 \times 10^5$ yr), D ($t = 1.2 \times 10^5$ yr), and E ($t = 4.1 \times 10^5$ yr), respectively. Dashed (A1) and dotted (A2) lines represent $t = 6 \times 10^4$ and 2×10^5 yr for model A.

$\Pi > 10^{-2}$, the amplitude of model E is less than that of model A at $t = 2 \times 10^5$ yr. This difference also comes from the fact that the post shock pressure of model E at $t_{\text{relax}} = 2.4 \times 10^4$ yr is less than that of model A at $t_{\text{relax}} = 3.3 \times 10^4$ yr.

Figure 6 shows the comparison of the square roots of the energy spectrum of the magnetic fields for the five models. For models A, C, and E, the curves take their maxima at ~ 51 pc. For models B and D, the peak sizes are 85 and 37 pc, respectively. This shows each spectrum has a peak near the scale of $1.5\lambda_0$ except for high-density model D. The peak magnitude of model A is 10^{-18} G, and that is twice as large as that of models B and C. For high-density model D, we can compare the result of model A at $t = 6 \times 10^4$ yr (A1, dashed line), both of which have a similar peak size. The peak wavelength of both models is 37 pc, although the amplitude of the magnetic fields of model D is twice as large as that of model A (A1). This difference seems to come from the fact that the magnetic fields are generated even in the inner region for model D since t/t_{relax} is larger compared with other models. This is also seen in the comparison of model E at $t = 4.1 \times 10^5$ yr and model A at $t = 2 \times 10^5$ yr (A2, dotted line). The

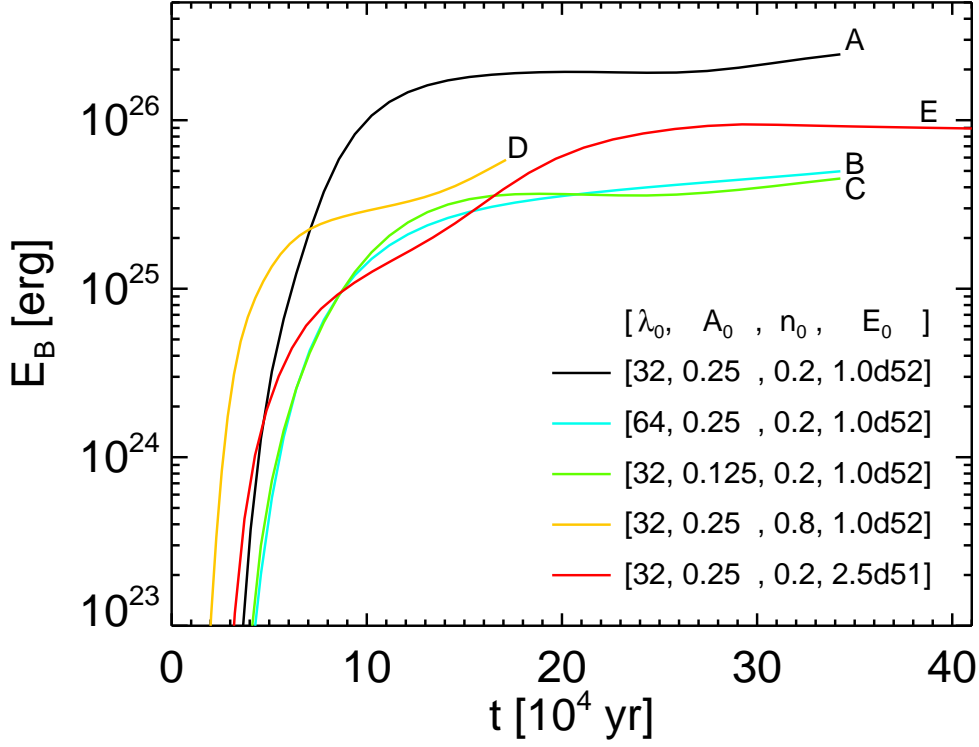


Fig. 7. Time evolution of the total magnetic energy produced by the Biermann mechanism for various models. Black, blue, green, yellow, and red lines represent models A, B, C, D, and E, respectively.

place of the peak wavelength of both models is 51 pc, and the peak energy density of model E is slightly lower than that of model A (A2).

For the coherence length, if the scale of the maximum energy density λ_{BP} is equal to $1.5\lambda_0$, the 3-dimensional length of toroidal magnetic field is estimated as $2\pi\lambda_{BP}/4 \sim 2\lambda_0$. This means that the coherence length of the toroidal field of 10^{-18} G is estimated as ~ 64 pc for models A, C, and E, while it is ~ 128 pc and ~ 32 pc for models B and D, respectively.

Time evolution of the total magnetic energy is shown in figure 7. The final magnetic energy for each model indicated by the figure is, $\sim 2 \times 10^{26}$ erg for model A, $\sim 5 \times 10^{25}$ erg for model B, $\sim 4 \times 10^{25}$ erg for model C, $\sim 6 \times 10^{25}$ erg for model D and $\sim 9 \times 10^{25}$ erg for model E, respectively. Apparent knees around $5 \times 10^4 - 2 \times 10^5$ yr come from the time scale of the electron temperature equilibrium shown in table 2. The total magnetic energy of model A is several times larger than those of other models. This behavior will be interpreted by an analytical estimation of the magnitude of the magnetic fields and the time evolution of the total energy in the next section. Although there are many uncertainties in our initial conditions, it is implied that the amplitude of the generated magnetic fields does not depend on SNR and ISM parameters so strongly.

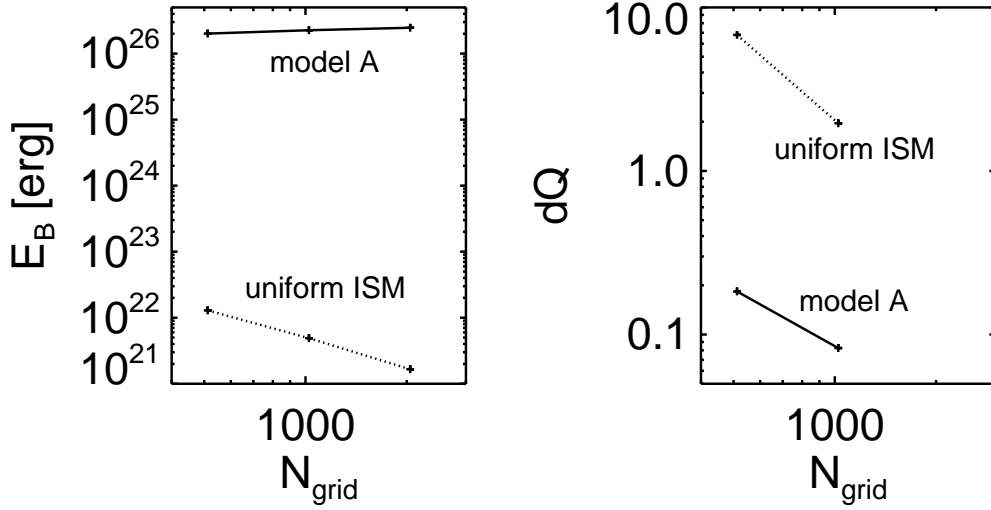


Fig. 8. Convergence study of total magnetic energy E_B (left panel) at 3.4×10^5 yr. dQ (right panel) means the relative convergence error in E_B of each model compared with the highest resolution model $N_{\text{grid}} = 2048$, defined as $dQ = |E_B(N_{\text{grid}}) - E_B(N_{\text{grid}} = 2048)| / E_B(N_{\text{grid}} = 2048)$. N_{grid} represents the number of grid points in one dimension and the spatial resolution of the simulation. Solid line means the result of the models which contain the inhomogeneity (model A), while dashed line means that of the models without the density fluctuation (uniform ISM).

Finally, let us argue the convergence of the results of our simulations. Figure 8 shows a convergence study in comparison with the simulations of lower spatial resolution in which the numerical box size is taken identically but the grid points are reduced as $N_{\text{grid}} = 512$ and 1024. E_B and dQ represent the total magnetic energy of SNR at 3.4×10^5 yr and the relative error in E_B of each low-resolution model compared with that of the highest resolution model $N_{\text{grid}} = 2048$, defined as $dQ = |E_B(N_{\text{grid}}) - E_B(N_{\text{grid}} = 2048)| / E_B(N_{\text{grid}} = 2048)$. In both panels, solid line is the result of the calculations of the interaction between the inhomogeneous ISM and SNR (model A) and dashed line is that of the evolution of SNR in uniform ISM. Left panel could be a measure of the numerical error in magnetic fields of our simulations. We can see that, in the highest resolution model, E_B of the model with homogeneous ISM is about 10^5 times smaller than that of model A and the numerical error of the magnetic fields generated by the curvature effect in the interior of SNR is negligible. In right panel, solid line shows that our simulation is almost converged and the difference is about 10% for the lower resolution model of $N_{\text{grid}} = 1024$. This indicates that roughly 128 grids for the radius of density fluctuation $r_0 = \lambda_0/4 = 8$ pc are required for a converged calculation.

4. Discussion

4.1. Characteristics of Magnetic Fields

In this subsection we give an order-of-magnitude estimation of the amplitude of the magnetic fields and the time evolution of the total magnetic energy generated by the Biermann mechanism. We extend the analysis in Hanayama et al. (2005) considering the time evolution of the physical quantities of the SNR bubble and the relaxation of the electron temperature. The characteristic pressure at the shock front is given by the ram pressure, $P \sim P_{\text{ram}} \sim (3/4)\rho_0 v_{\text{bub}}^2$, and its gradient is estimated as $\nabla P \sim P/L$ where the pressure scale height can be evaluated as a typical shell width $L \sim R_{\text{bub}}/10$. Noting that the density gradient is determined by the fluctuation of ISM, we have $\nabla \rho \sim A_0 \rho_0 / (2r_0) = 2A_0 \rho_0 / \lambda_0$. Thus, the amplitude of magnetic fields generated within a characteristic time, $\tau \sim L/v_{\text{bub}}$, is given by (see equation (8))

$$\begin{aligned} B_{\text{Bier}} &= \left| \alpha \frac{\nabla P \times \nabla \rho}{\rho^2} \tau \right| \\ &\sim \alpha \frac{3v_{\text{bub}} A}{2\lambda_0} \sim \frac{3\alpha A}{5\lambda_0} \left(\frac{E_0}{\rho_0} \right)^{1/5} t^{-3/5} \\ &\sim 10^{-17} \text{ G} \left(\frac{\lambda_0}{32 \text{ pc}} \right)^{-1} \left(\frac{A}{0.5} \right) \left(\frac{n_0}{0.2 \text{ cm}^{-3}} \right)^{-1/5} \\ &\quad \times \left(\frac{E_0}{10^{52} \text{ erg}} \right)^{1/5} \left(\frac{t}{10^5 \text{ yr}} \right)^{-3/5}, \end{aligned} \quad (31)$$

where we used equation (19) and put $\alpha \sim 0.5 \times 10^{-4} \text{ G sec}$. This is reasonably consistent with the value obtained from our numerical simulations.

On the other hand, the growth of the total magnetic energy during a time interval in which an SNR expands from volume V to $V + dV$ can be estimated as

$$\begin{aligned} dE_B &\sim \frac{B_{\text{Bier}}^2}{8\pi} dV \sim \frac{B_{\text{Bier}}^2}{8\pi} 4\pi R^2 dR \\ &\sim \frac{9\alpha^2 A^2 E_0}{125\lambda_0^2 \rho_0} t^{-1} dt, \end{aligned} \quad (32)$$

where $dV (= 4\pi R^2 dR)$ is a difference in the volume of SNR between two epochs t and $t + dt$ and we used equation (18). The total magnetic energy $E_B(t)$ contained in a SNR of the age t is given by the time integration of $dE_B(t)/dt$ from t_{start} to t . Assuming $t_{\text{start}} \sim t_{\text{relax}}$ for the sufficient equilibrium of the inner region, we obtain the total magnetic energy as

$$\begin{aligned} E_B(t) &\sim \int_{t_{\text{start}}}^t \frac{9\alpha^2 A^2 E_0}{125\lambda_0^2 \rho_0} t^{-1} dt \\ &= \frac{9\alpha^2 A^2 E_0}{125\lambda_0^2 \rho_0} (\ln t - \ln t_{\text{start}}) \\ &\sim 3 \times 10^{26} \text{ erg} \left(\frac{\lambda_0}{32 \text{ pc}} \right)^{-2} \left(\frac{A}{0.5} \right)^2 \left(\frac{n_0}{0.2 \text{ cm}^{-3}} \right)^{-1} \end{aligned}$$

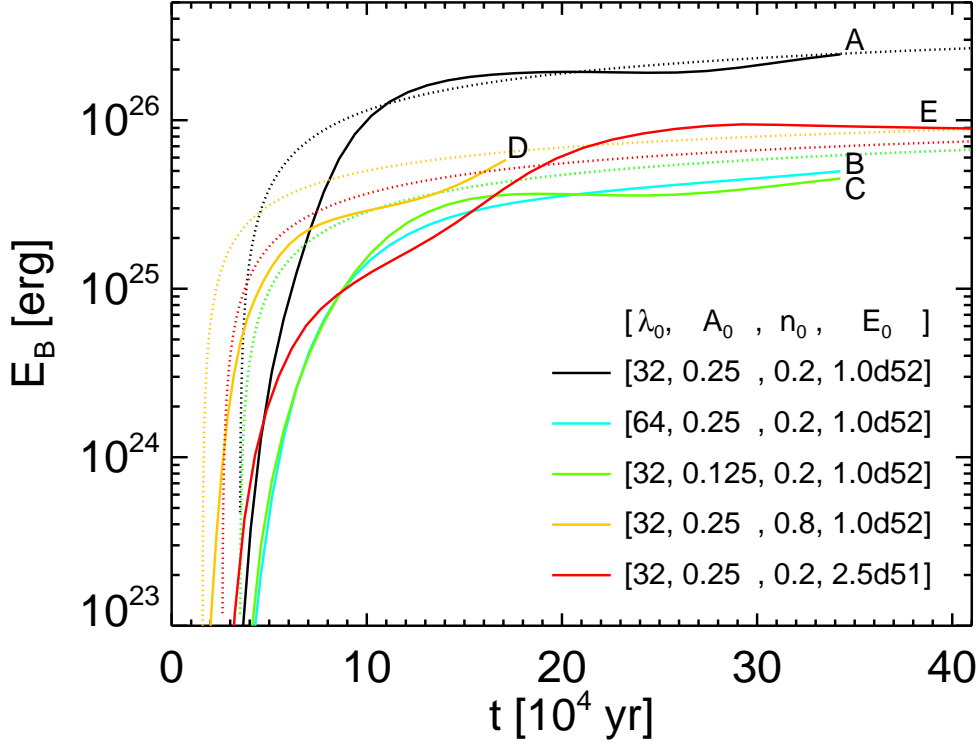


Fig. 9. The same as figure 7 but added lines of the analytic estimation obtained from equation (33). Black, blue, yellow, orange and red lines represent models A, B, C, D, and E, respectively. Solid and dotted lines represent the numerical result and the analytic estimation.

$$\times \left(\frac{E_0}{10^{52} \text{ erg}} \right) \ln \left(\frac{t/t_{\text{relax}}}{10} \right). \quad (33)$$

See table 2. This analytic estimation is also plotted in figure 9 to compare with our numerical simulation. Consistency between these estimations and the numerical results is remarkable, explaining not only the qualitative behavior but also the absolute magnitudes.

4.2. Implication for Seed Magnetic Fields

Now we estimate the spatially-averaged energy density of the magnetic fields in proto-galaxies expected from the first star SNR and consider whether they could be a source of the seed fields or not.

The total number density of the SNe is roughly estimated as

$$n_{\text{SN}} \simeq \frac{\dot{\rho}_{\star, \text{III}} \tau}{M_{\text{S}}}, \quad (34)$$

where $\dot{\rho}_{\star, \text{III}}$, τ , and M_{S} are the primordial star formation rate (SFR) of Pop III stars per unit volume, the duration of the first star formation and a typical mass of the first stars, respectively. As for the SFR of Pop III stars, extrapolating the one by Pelló et al. (2004) and Ricotti et al.

(2004), we have

$$\dot{\rho}_{*,\text{III}} \sim 6 \times 10^{-4} M_{\odot} \text{ yr}^{-1} \text{ Mpc}^{-3} \left(\frac{f_{\text{III}}}{0.06} \right), \quad (35)$$

where f_{III} is the fraction of the Pop III stars in SFR, and we adopt $f_{\text{III}} = 0.06$ that was derived under the assumption that very massive black holes produced from first stars end up in supermassive black holes in galactic centers (Schneider et al., 2002). If we assume the formation period of the first stars continued from $z \sim 20$ to 10 ($\tau \sim 0.3$ Gyr), the total number density of the Pop III SNe can be estimated as

$$n_{\text{SN}} \sim 4 \times 10^{-68} \text{ cm}^{-3} \left(\frac{1+z}{11} \right)^3 \left(\frac{\dot{\rho}_{*,\text{III}}}{6 \times 10^{-4} M_{\odot} \text{ yr}^{-1} \text{ Mpc}^{-3}} \right) \\ \times \left(\frac{\tau}{0.3 \text{ Gyr}} \right) \left(\frac{M_{\text{S}}}{200 M_{\odot}} \right)^{-1}, \quad (36)$$

where the number density is in units of physical scale, not comoving. Primordial star formation rate was also estimated by Greif & Bromm (2006). Even taking Pop III and Pop II.5 of their classification into account, we confirmed that our results below do not change so much.

Taking the typical value of the magnetic energy of a Pop III SNR as that of model A, $E_B \sim 10^{26}$ erg, the spatially-averaged magnetic energy density is estimated as, $e_B \sim 10^{-42}$ erg cm $^{-3}$. If we assume that galaxies are formed in such a magnetized medium, the magnetic energy density in protogalaxies is given by

$$e_{B,\text{gal}} \sim e_B \Delta^{4/3} \\ \sim 10^{-39} \text{ erg cm}^{-3} \left(\frac{\Delta}{200} \right)^{4/3} \left(\frac{e_B}{10^{-42} \text{ erg cm}^{-3}} \right), \quad (37)$$

where Δ represents the overdensity of protogalaxies. This means that the average magnitude of the magnetic fields becomes $B \sim 10^{-19}$ G, which would be enough for the required seed field of galactic dynamo (Lesch & Chiba, 1995). Although the coherence length of the order of 10 – 100 pc estimated here is much smaller than the galactic scale, it would be amplified by the galactic dynamo (Poezd et al., 1993; Beck et al., 1994, 1996). It may also be amplified by interstellar turbulence dynamo to produce fluctuating components (Balsara et al., 2004).

Finally let us comment on the three-dimensional effects. In this study, we performed two-dimensional MHD simulations. However, because of the assumption of the axisymmetry, the generated magnetic fields are restricted to the toroidal component. This makes it rather hard to argue the coherence length of magnetic fields. Further, the spectrum of magnetic fields would be different in three-dimensional simulations, because the vorticity cascade is different in 2D and 3D turbulences. We will present three-dimensional simulations in a separate paper but we believe that most of the features of the Biermann mechanism in SNR are captured in the present study.

5. Summary

In this article, we argued the Biermann mechanism in primordial supernova remnants through two-dimensional MHD simulations with the Biermann term. We solved simultaneously the relaxation of the electron temperature, which is crucial to the efficiency of the Biermann mechanism and was not taken into account in our previous study (Hanayama et al., 2005). It was found that magnetic fields begin to be generated from $t = t_{\text{relax}}$ just behind the shock front. The total magnetic energy reaches about 10^{26} erg and does not depend strongly on the parameters of SNR and ISM. We could understand analytically the dependence of the magnetic total energy on the parameters and also the time evolution. Finally we evaluated the expected amplitude of magnetic fields in protogalaxies, which would be sufficient for seed fields of the observed galactic magnetic fields.

HH would like to express sincere thanks to Prof. Tomoyuki Hanawa, Dr. Tomoaki Matsumoto, Dr. Kazuya Saigo, Dr. Dai G. Yamazaki, and Dr. Motohiko Kusakabe for helpful advice on technical problems in numerical works and encouragement. HH also thanks Prof. Ryoji Matsumoto and Dr. Takaaki Yokoyama for a contribution to the calculation code, CANS (Coordinated Astronomical Numerical Software). Numerical computations were carried out on Cray XT4 and NEC SX9 systems at the Center for Computational Astrophysics of NAOJ, and NEC SX8 system at Yukawa Institute for Theoretical Physics, Kyoto University. Keitaro Takahashi is supported in part by MEXT Grant-in-Aid for the global COE programs "Quest for Fundamental Principles in the Universe: from Particles to the Solar System and the Cosmos" at Nagoya University. A part of this work (Tomisaka) was supported from Grant-in-Aid for Scientific Research (17340059) from MEXT.

References

- Abel, T., Bryan, G. L., & Norman, M. L. 2002, *Science*, 295, 93
- Balsara, D., Benjamin, R. A., & Cox, D. P. 2001, *ApJ*, 563, 800
- Balsara, D. S., Kim, J., Mac Low, M., & Mathews, G. J. 2004, *ApJ*, 617, 339
- Bamba, K., & Yokoyama, J. 2004, *Phys. Rev. D*, 69, 043507
- Beck, R., Poezd, A. D., Shukurov, A., & Sokoloff, D. 1994, *A&A*, 289, 94
- Beck, R., Brandenburg, A., Moss, D., Shukurov, A., & Sokoloff, D. 1996, *ARA&A*, 34, 155
- Biermann L. 1950 *Z. Naturforsch*, 5a, 65
- Brio M., Wu C. C. 1988, *J. Comput. Phys.*, 75, 400
- Cargo, P., & Gallice, G. 1997, *J. Comput. Phys.*, 136, 446
- Christensson, M., Hindmarsh, M., & Brandenburg, A. 2001, *Phys. Rev. E*, 64, 056405
- Cui, W., & Cox, D. P. 1992, *ApJ*, 401, 206
- Cox, D. P. 1972, *ApJ*, 178, 159
- Cox, D. P., & Anderson, P. R. 1982, *ApJ*, 253, 268
- Dedner, A., Kemm, F., Kröner, D., Munz, C.-D., Schnitzer, T., & Wesenberg, M. 2002, *J. Comput. Phys.*, 175, 645
- Fryer, C. L., Woosley, S. E., & Heger, A. 2001, *ApJ*, 550, 372
- Gnedin, N. Y., Ferrara, A., & Zweibel, E. G. 2000, *ApJ*, 539, 505
- Greif, T. H., & Bromm, V. 2006, *MNRAS*, 373, 128
- Greif, T. H., Johnson, J. L., Bromm, V., & Klessen, R. S. 2007, *ApJ*, 670, 1
- Hanayama, H., Takahashi, K., Kotake, K., Oguri, M., Ichiki, K., & Ohno, H. 2005, *ApJ*, 633, 941
- Hirsch, C. 1990, *Numerical Computation of Internal and External Flows*, Vol. 2 (Chichester, England and New York: John Wiley & Sons)
- Ichiki, K., Takahashi, K., Ohno, H., Hanayama, H., & Sugiyama, N. 2006, *Science*, 311, 827
- Ichiki, K., Inoue, S., & Takahashi, K. 2008, *ApJ*, 682, 127
- Itoh, H. 1978, *PASJ*, 30, 489
- Itoh, H. 1984, *ApJ*, 285, 601
- Kato, T. N., & Takabe, H. 2008, *ApJL*, 681, L93
- Kitayama, T., & Yoshida, N. 2005, *ApJ*, 630, 675
- Klein, R. I., McKee, C. F., & Colella, P. 1994, *ApJ*, 420, 213
- Kulsrud, R. M., Cen, R., Ostriker, J. P., & Ryu, D. 1997, *ApJ*, 480, 481
- Kulsrud, R. M., Zweibel, E. G. 2008, *Rept. Prog. Phys.*, 71, 046901
- Langer, M., Aghanim, N., & Puget, J.-L. 2005, *A&A*, 443, 367
- Lesch, H., & Chiba, M. 1995, *A&A*, 297, 305
- Masai, K. 1994, *ApJ*, 437, 770
- Matsumoto, T. 2007, *PASJ*, 59, 905
- Miranda, O. D., Opher, M., & Opher, R. 1998, *MNRAS*, 301, 547

- Nakamura, F., McKee, C. F., Klein, R. I., & Fisher, R. T. 2006, *ApJS*, 164, 477
- Nishikawa, H., & Kitamura, K. 2008, *J. Comput. Phys.*, 227, 2560
- Pelló, R., Schaerer, D., Richard, J., Le Borgne, J.-F., & Kneib, J.-P. 2004, *A&A*, 416, L35
- Plaga, R. 1995, *Nature*, 374, 430
- Poezd, A., Shukurov, D., & Sokoloff, D. 1993, *MNRAS*, 264, 285
- Rakowski, C. E. 2005, *Advances in Space Research*, 35, 1017
- Ricotti, M., Haehnelt, M. G., Pettini, M., & Rees, M. J. 2004, *MNRAS*, 352, L21
- Roe, P. L. 1981, *J. Comput. Phys.*, 43, 357
- Schneider, R., Ferrara, A., Natarajan, P., & Omukai, K. 2002, *ApJ*, 571, 30
- Sedov L. I. 1959, “Similarity and Dimensional Methods in Mechanics,” (New York: Academic Press)
- Shimada, N., & Hoshino, M. 2000, *ApJL*, 543, L67
- Shull, J. M. 1980, *ApJ*, 237, 769
- Slavin J. D., Cox D. P. 1992, *ApJ*, 392, 131
- Spitzer, L. 1962, *Physics of Fully Ionized Gases*, 2nd edition, (New York: Wiley-Interscience)
- Takahashi, K., Ichiki, K., Ohno, H., & Hanayama, H. 2005, *Phys. Rev. Lett.*, 95, 121301
- Takahashi, K., Murase, K., Ichiki, K., Inoue, S., & Nagataki, S. 2008, *ApJL*, 687, L5
- Turner M. S. and Widrow, L. M. 1988, *Phys. Rev. D*, 37, 2743.
- Widrow, L. M. 2002, *Rev. Mod. Phys.*, 74, 775
- Wise, J. H., & Abel, T. 2008, *ApJ*, 684, 1
- Xu, H., O’Shea, B. W., Collins, D. C., Norman, M. L., Li, H., & Li, S. 2008, *ApJL*, 688, L57